Galactic Cosmic Ray Energy Spectra for Heavy Elements (Ne to Zn) from ~0.8 to ~10 GeV/nuc with the SuperTIGER Instrument

A. W. Labrador[1],[*], W. R. Binns[2], R. G. Bose[2], T. J. Brandt[3], P.F. Dowkontt[2], T. Hams[3],[4], M. H. Israel[2], J. T. Link[3],[4], R. A. Mewaldt[1], J. W. Mitchell[3], R. P. Murphy[2], B. F. Rauch[2], K. Sakai[3],[4], M. Sasaki[3],[4], E. C. Stone[1], C. J. Waddington[5], N.E. Walsh[2], J. E. Ward[2], and M. E. Wiedenbeck[6]

1. California Institute of Technology, Pasadena, CA 91125 USA

2. Washington University, St. Louis, MO 63130 USA

3. NASA/Goddard Space Flight Center, Greenbelt, MD 20771 USA

4. Center for Research and Exploration in Space Science and Technology (CRESST), Greenbelt, MD 20771, USA

5. The University of Minnesota, Minneapolis, MN 55455, USA

6. Jet Propulsion Laboratory, California Institute of Technology, Pasadena, CA 91109 USA

* E-mail: labrador@srl.caltech.edu

SuperTIGER (Trans-Iron Galactic Element Recorder) is a large-area balloon-borne instrument built to measure the galactic cosmic-ray (GCR) abundances of elements from Z=10 (Ne) through Z=56 (Ba) at energies from ~0.8 to ~10 GeV/nuc. SuperTIGER flew over Antarctica for a record-breaking 55 days, from December 8, 2012 to February 1, 2013. We will report progress on calculations of galactic cosmic ray spectra corrected to the top of the atmosphere for abundant elements between Ne and Zn from the SuperTIGER flight data. The energy spectra calculations will include up to date refinements to the energy calibrations for the acrylic and aerogel Cherenkov detectors in the instrument, and we will report on new instrument and atmospheric corrections to the top of the atmosphere for energies and abundances.

Heinz and Sunyaev (2002) suggested that microquasar jets like those observed in GRS 1915+105 and GRO J1655-40 may be observable as near monoenergetic peaks in heavy ion spectra in the 3-10 GeV/nuc energy range. The large area and long flight duration of SuperTIGER is particularly suited to looking for these microquasar signatures with good statistics. We will compare our SuperTIGER spectra with ACE/CRIS and HEAO-3 spectra and with model GCR spectra solar modulated for the time period of the flight, and we will search for features that may be produced by microquasar jets.

36th International Cosmic Ray Conference -ICRC2019-
July 24th - August 1st, 2019
Madison, WI, U.S.A.

1.   Introduction

SuperTIGER (the Trans-Iron Galactic Element Recorder) is a large area, balloon-borne experiment designed and flown to measure the galactic cosmic-ray abundances of elements from Ne (Z=10) to Ba (Z=56) at ~0.8–10 GeV/nuc. SuperTIGER had a record-breaking flight of 55 days around Antarctica, from December 8, 2012 to February 1, 2013 [1].

We have previously reported relative abundances of ultraheavy elements (30≤Z≤40) in SuperTIGER data, and these results are consistent with galactic cosmic ray origins in OB associations with preferential acceleration of refractory elements over volatile elements [2]. Additionally, relative abundances of iron secondaries measured by SuperTIGER, e.g. (Sc+Ti+V)/Fe, are consistent with HEAO measurements as well as Standard Leaky Box Model calculations [3,4].

In addition to measuring relative abundances of ultraheavy elements and abundant elements, SuperTIGER measures energy spectra for abundant elements (Z<30). Heinz and Sunyaev [5] suggested that relativistic jets observed in some micro-quasars (e.g. GRS 1915+105 and GRO J1655-40) might produce narrow, near-monoenergetic features in cosmic ray spectra. Figure 1 shows simulated SuperTIGER Fe energy spectra with simulated, near-monoenergetic beams appearing as 1%, 5%, and 10% integrated enhancements above a normal power-law spectrum.
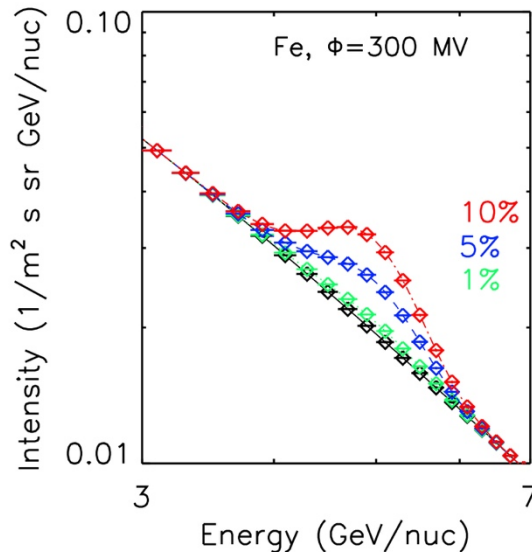

Figure 1: Example of near monoenergetic Fe superimposed atop a normal galactic Fe spectrum. The measurements are simulated for the 2012-2013 SuperTIGER flight. The colored curves represent 1, 5, and 10% integrated enhancements above the normal Fe spectrum integrated from 2.5 to 10 GeV/nuc, and the black curve is the simulated interstellar spectrum solar modulated with a 300 MV modulation parameter.

We report in this paper our current progress in measuring the ~0.8–10 GeV/nuc spectra for several elements from Ne to Fe from the SuperTIGER flight data.

2. The SuperTIGER Instrument

The SuperTIGER payload is divided into two nearly identical modules, each of which is composed of a stack of several detectors. From top to bottom, the detectors in each module are a plastic scintillator (S1), a top scintillating optical fiber hodoscope (H1), an aerogel Cherenkov (refractive index n=1.025 or n=1.043) detector (C0), an acrylic Cherenkov (n=1.49) detector (C1), another plastic scintillator (S2), a bottom hodoscope (H2), and a third plastic scintillator (S3). In one module, the aerogel blocks in the C0 detector are entirely n=1.043 refractive index aerogels (threshold energy of ~2.5 GeV/nuc), while in the other module, half of the C0 aerogels have a refractive index n=1.043 while the other half have n=1.025 (threshold energy ~3.3 GeV/nuc). Otherwise, the modules are functionally identical. See Figure 2.

Particles are identified individually by charge (Z), via the scintillator signals, and velocity, via the Cherenkov signals. Particle data are stored in onboard solid state drives as well as transmitted via line-of-sight (LOS) telemetry or TDRSS satellite.

The SuperTIGER instrument is described in detail by Binns et al. [2].
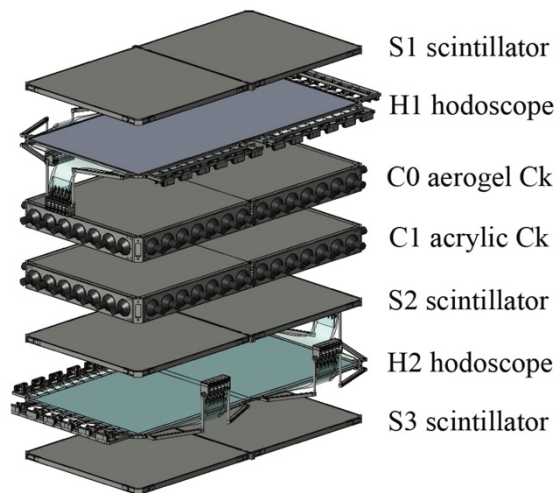

Figure 2: Expanded view of one SuperTIGER module, from Binns et al. [2].

3. Data Analysis

For this analysis, we use the SuperTIGER flight TDRSS data from 15 December 2012 through 2 February 2013. For Cherenkov calibration, we use 26-28 December 2012 line-of-sight (LOS) data telemetered when the experiment could transmit data directly to McMurdo Base. Though a small data set, the LOS data was not processed through the priority system that was employed for the TDRSS data, which means that the LOS data is more complete for Z<30 during its duration.

Particles are identified by charge and velocity through combinations of measurements in the scintillation and Cherenkov detectors (Figures 3a and 3b). The hodoscopes provide particle

trajectories for angle- and position-dependent mapping and correction in the data analysis. The axes in Figures 3a and 3b are the scintillator ($S^{1/1.7}$) and Cherenkov ($C0^{1/2}$ and $C1^{1/2}$) signals, scaled to approximately Z for each element at the highest velocities. Element tracks for abundant elements are easily identifiable in each figure, with Fe being the darkest track toward the top of each figure and Mg, Al, and Si tracks being visible near the bottom. Ne is partly visible in the lower energy range (Figure 3a), but it is less visible in the higher energy range (Figure 3b) due to it being below the scintillator signal dynamic range used in the data selection criteria.

From the abundant element tracks, charges for ultraheavy elements (Z≥30) may be extrapolated. More rigorous charge determination for the ultra-heavy elements is described in detail by Murphy et al. [2] and Walsh et al. [6].
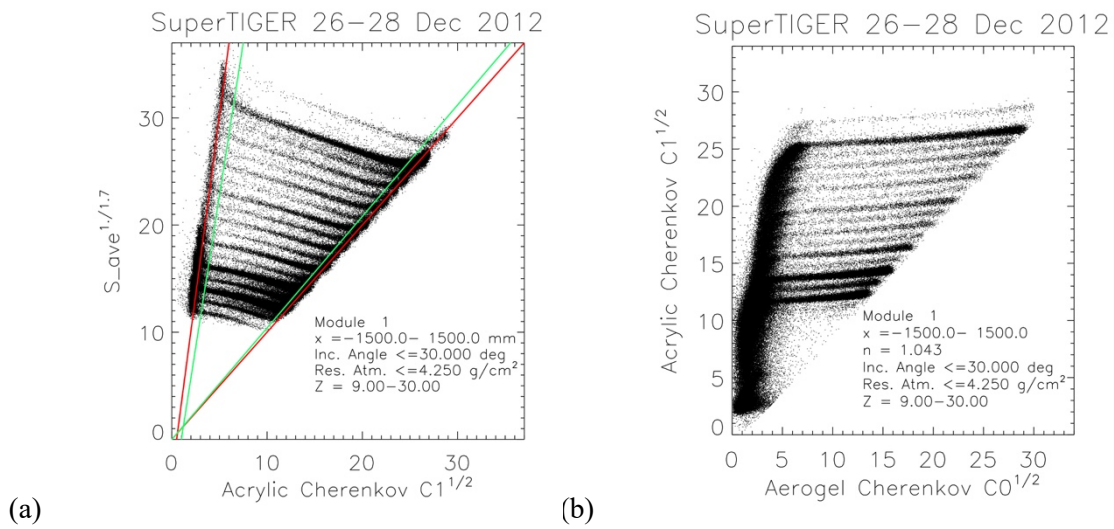
Figures 3 a (left) and b: Scintillation signal vs. acrylic Cherenkov signal and acrylic Cherenkov signal vs. aerogel Cherenkov signal.

Abundant elements are identified by charge separation from the data shown in Figures 3a and 3b, and we obtain velocity ß from the Cherenkov signals with the formula

$$C_{norm} = Z^2 \left[\frac{1 - \frac{1}{\beta^2 n^2}}{1 - \frac{1}{n^2}} \right]$$ [1]

where Z is the particle charge, n is the Cherenkov radiator index of refraction, and ß is the particle velocity. C_{norm} is the Cherenkov signal, which is expected to vary from 0 to Z^2, depending upon the energy and exceeding zero only when the threshold velocity $\beta_{thresh} = 1/n$ is exceeded.

When scaling to the arbitrary scales shown on Figures 3a and 3b, account must be taken of the zero offsets and background at the threshold signal. The background signals contributing to the zero offsets include scintillation signal from mounting or reflecting materials in the Cherenkov counters as well as secondary Cherenkov signals from Goretex reflector and from knock-on electrons. In both Figures 3a and 3b, the rightmost boundaries of the data are defined by the

maximum Cherenkov signals in C1 and C0, or maximum velocity $\beta \approx 1$. The left boundaries are defined by background signals below the primary Cherenkov radiator threshold, e.g. dominated by scintillation ($\propto Z^2$) in the C1 counter (Figure 3a), and a combination of scintillation (from the thin polyethylene film used to mount the aerogels), Cherenkov signals from knock-on electrons in the aerogels, and Goretex reflector Cherenkov signals in C0.

Figure 3a shows that the establishment of a velocity scale is straightforward, with left and right boundaries of the data defining threshold velocity (ß=1/1.49, or energy 0.33 GeV/nuc at the instrument; zero C0 signal) and the right boundary marking $\beta \approx 1$ in the acrylic Cherenkov signal. These boundaries are marked with red lines in Figure 3a. However, at the upper end of this energy range in Figure 3a, the energies overlap with the aerogel Cherenkov threshold (~2.4 GeV/nuc). To simplify the current analysis, we drop the ~2.0-2.6 GeV/nuc energy bins. Near or below acrylic Cherenkov threshold, particle signals overlap between adjacent charge values (Z). Therefore, events outside of the boundaries marked by the green lines in Figure 3a are either discarded, at low energies, or are analyzed instead with the aerogel Cherenkov signals providing velocity.

(a)   (b)
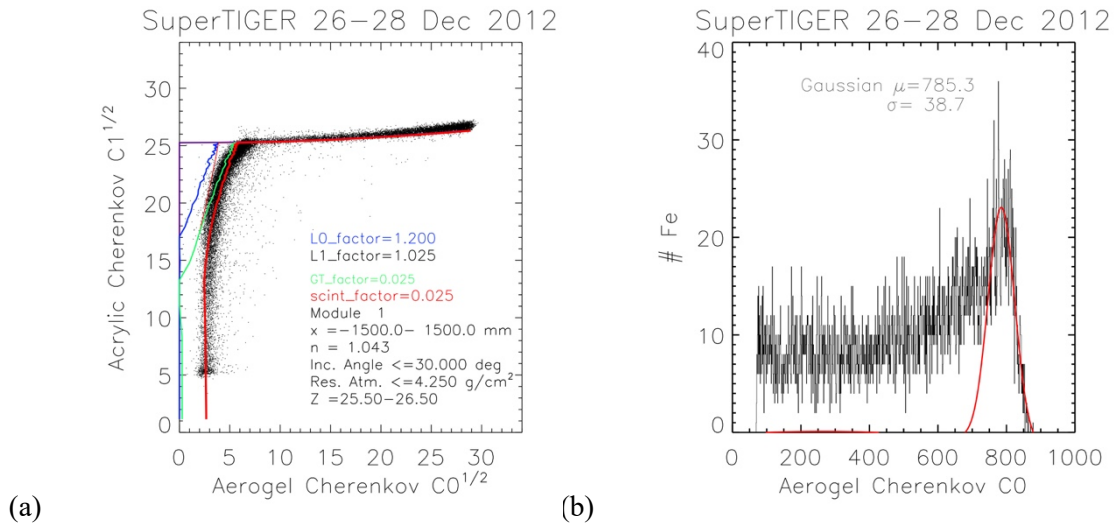
Figures 4a (left) and 4b: At left are SuperTIGER Fe data points, plotted as acrylic Cherenkov signal vs. aerogel Cherenkov signal. Fits of below-threshold background contributions are shown, including scintillation (bold red) from the plastic film containing the aerogel, Goretex Cherenkov signal (red without knock-on electrons, green with knock-on electrons), and the aerogel Cherenkov signal (with (purple) and without (blue) knock-on electrons). At right is a Gaussian fit to the aerogel Cherenkov signal histogram for Fe at ß=1.

Figures 4a and 4b illustrate how the velocity scales are established in the aerogel Cherenkov energy range. Figure 4a shows SuperTIGER data points for Fe, plotted as acrylic Cherenkov signal vs. aerogel Cherenkov signal. Contributions from scintillation from the plastic film used to wrap and mount the aerogels are shown as the yellow curve, while Cherenkov light

contributions from the Goretex reflector material are shown in red (and green, with knock-on electron signals in the Goretex). The primary aerogel Cherenkov signal is shown in purple, with dark blue showing the knock-on electron contribution from the aerogels. (For all knock-on electron Cherenkov contributions, we used a Monte Carlo simulation derived from calculations by Grove & Mewaldt [7].) Finally, Figure 4b shows a Gaussian fit to the uppermost end of the Fe Cherenkov signal, yielding the $\beta \approx 1$ signal.

Similar calibration was employed in this analysis for S, Si, and Mg, and it was attempted for Ne. The fitted thresholds and $\beta \approx 1$ limits in $\sqrt{C0}$ are linear vs. Z, as reflected in Figure 3b.
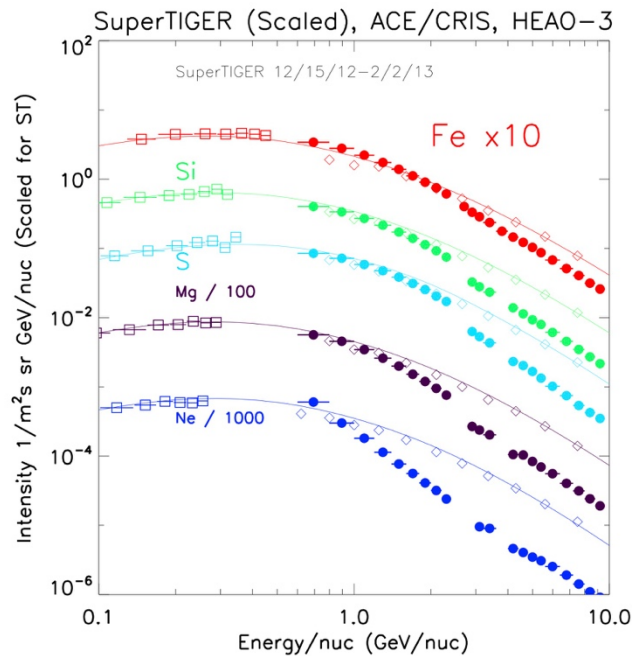
4. Results

Figure 5: Scaled SuperTIGER data spectra for Fe, S, Si, Mg, and Ne (closed circles) for the 2012-2013 flight. ACE/CRIS intensities (open triangles squares) for the same period are shown [8], with a 1 AU galactic cosmic ray model calculation with a solar modulation parameter $\phi = 575\ MV$. HEAO-3 data are shown as open diamonds [4]. Statistical uncertainties are included but are smaller than the plot symbols; systematic uncertainties await further analysis.

Analysis for the SuperTIGER 2012-2013 flight is ongoing. We have refined energy calibrations and extended them to lower Z, as discussed in Section 3. We have calculated energy bin-shifting through the detector stacks, but interaction loss corrections from a recently-developed GEANT4 simulation of the SuperTIGER instrument were not completed in time for this paper. In addition, a livetime calculation for the flight as well as instrument efficiency analysis (e.g. from the priority system, altitude variation, and telemetry) remain to be completed. Therefore, we report here SuperTIGER intensities measured at the instrument and then scaled to approximate

the top-of-the-atmosphere results measured by ACE/CRIS and HEAO-3. Scaling is also different for the three different Cherenkov energy ranges (below n=1.043 threshold, between n=1.043 and n=1.025 thresholds, and above n=1.025 threshold), resulting from different geometry factors as well as instrument efficiency.

Figure 5 compares SuperTIGER intensities for Fe, S, Si, and Mg for the 2012-2013 flight with ACE/CRIS intensities at the same time period, a 1 AU galactic cosmic ray model solar modulated to 575 MV, and high energy HEAO-3 data [4,8,9]. Ne is also attempted. Additional scaling factors by powers of 10 are also applied and indicated, in order to separate elements. Results for Fe show a reasonable approximation for the HEAO data, with deviations increasing with increasing energy and decreasing element charge. Further analysis will determine to what extent those deviations remain after the instrument and atmospheric corrections are applied.
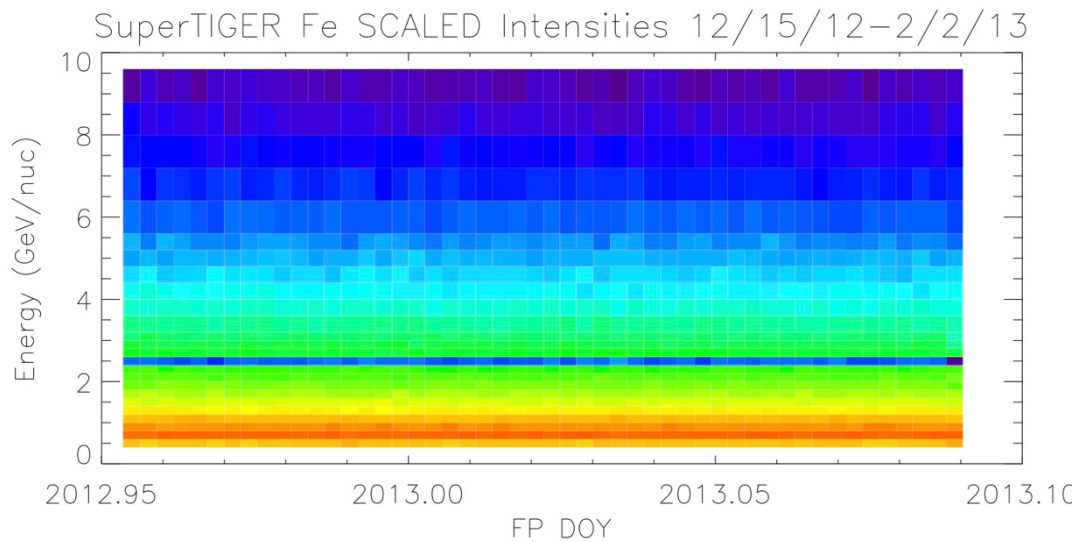

Figure 6: Scaled SuperTIGER Fe intensities vs. time, for the 2012-2013 flight. The color scale is logarithmic in scaled intensity.

Figure 6 is a plot of scaled SuperTIGER Fe spectra vs. time, binned daily. The daily spectra were normalized so that each integrated spectrum matched that of the first day, 15 December 2012, in order to correct for variations in count rate due to telemetry in TDRSS and changes in altitude (or atmospheric overburden). Colors are assigned to a logarithmic scale in particle intensity. The dark band at ~2.5 GeV/nuc is the energy bin that is dropped (or minimized) around to the C1-C0 overlap; it shows variations due to the time-dependent normalization scaling. Above 3 GeV/nuc, no large enhancements indicative of an intense near-monoenergetic beam from a nearby microquasar is evident.

Acknowledgements

References

[1] W.R. Binns et al, The SuperTIGER Instrument: Measurements of Elemental Abundances of Ultra-Heavy Galactic Cosmic Rays, The Astrophysical Journal **788** 18 (June 2014).

[2] R. Murphy et al., *Abundances of Ultra-Heavy Galactic Cosmic Rays from the SuperTIGER Instrument*, Proc. 34th International Cosmic Ray Conference, The Hague (2015).

[3] A.W. Labrador et al., Galactic Cosmic-Ray Composition and Spectra for Ne through Cu from 0.8 to 10 GeV/nuc with the SuperTIGER Instrument, Proc. 34th International Cosmic Ray Conference, The Hague (2015).

[4] J.J. Engelmann et al., Charge composition and energy spectra of cosmic-ray nuclei for elements from Be to Ni. Results from HEAO-3-C2, Astronomy and Astrophysics **233** 96 (1990).

[5] S. Heinz & R. Sunyaev, Cosmic rays from microquasars: A narrow component to the CR spectrum?, Astronomy and Astrophysics, **390** 751 (2002).

[6] N.E. Walsh et al., Proc. 36th International Cosmic Ray Conference, Madison (2019). *These Proceedings.*

[7] J.E. Grove and R.A. Mewaldt. Nuclear Instruments and Methods in Physics Research, **A314**, 495 (1992).

[8] ACE Science Center, http://www.srl.caltech.edu/ACE/ASC/level2/index.html.

[9] A.J. Davis, R.A. Mewaldt, W.R. Binns, E.R. Christian, C.M.S. Cohen, A.C. Cummings, J.S. George, P.L. Hink, R.A. Leske, E.C. Stone, T.T. von Rosenvinge, M.E. Wiedenbeck, N.E. Yanasak, *Proceedings of the 27th International Cosmic Ray Conference, Hamburg,* **10**, 3971, 2001.